

# CAVITIES OF CRYSTAL LIGHT

©IMAGESTATE

*By P. Bhattacharya,  
J. Sabarinathan,  
W-D. Zhou, P-C. Yu,  
and A. McGurn*

## Electrically Injected Photonic Crystal Microcavity Light Sources May Realize High-Efficiency Single-Mode LEDs

**T**his article presents the characteristics of photonic crystal microcavity light sources. Microcavities with dimensions on the scale of the wavelength of light are being extensively investigated due to their ability to exhibit enhanced spontaneous emission, directional output, and single-mode operation. Photonic crystals, which are the optical analog of semiconductors in electronic devices, are capable of controlling the properties of light by confining photons in one, two, or three dimensions. The technology to fabricate photonic crystals at the optical-wavelength scale (i.e., feature sizes at the submicron scale) has only very recently been achieved. Single or multiple defects in the photonic crystals act as microcavities with dimensions on the order of the wavelength of light and have emerged as the preferred way to obtain defect-free optical microcavities.

Several groups around the world are actively pursuing photonic crystal applications, especially 2-D photonic crystals, and have demonstrated optically pumped microcavities. At the

University of Michigan, Ann Arbor, we have been investigating electrically injected photonic crystal microcavities, and these devices are described in this article. Electrically injected microcavities offer the advantage of possible integration with current optoelectronic circuits and devices. Also, arrays of such devices can be fabricated when electrically controlled.

### Overview

In bulk material, or in a large cavity, the photon density of states is a monotonic function and spontaneous emission occurs into a large number of states, which occupy a spectral region much larger than the spontaneous emission linewidth. In a conventional laser made of such materials, significant stimulated emission output can only be obtained when the input power crosses a threshold to overcome the free-space loss. In a wavelength-sized microcavity [1]-[3], formed by 1-, 2-, or 3-D photon-mode confinement, a single spectrally distinct mode, determined by the microcavity dimensions, can receive most or all of the spontaneous emission. By applying

Fermi's golden rule, it has been shown that the rate of spontaneous emission is enhanced in such a microcavity, due to the change in the mode density [2], [4]. The spatial profile of the spontaneous emission also becomes vertically collimated.

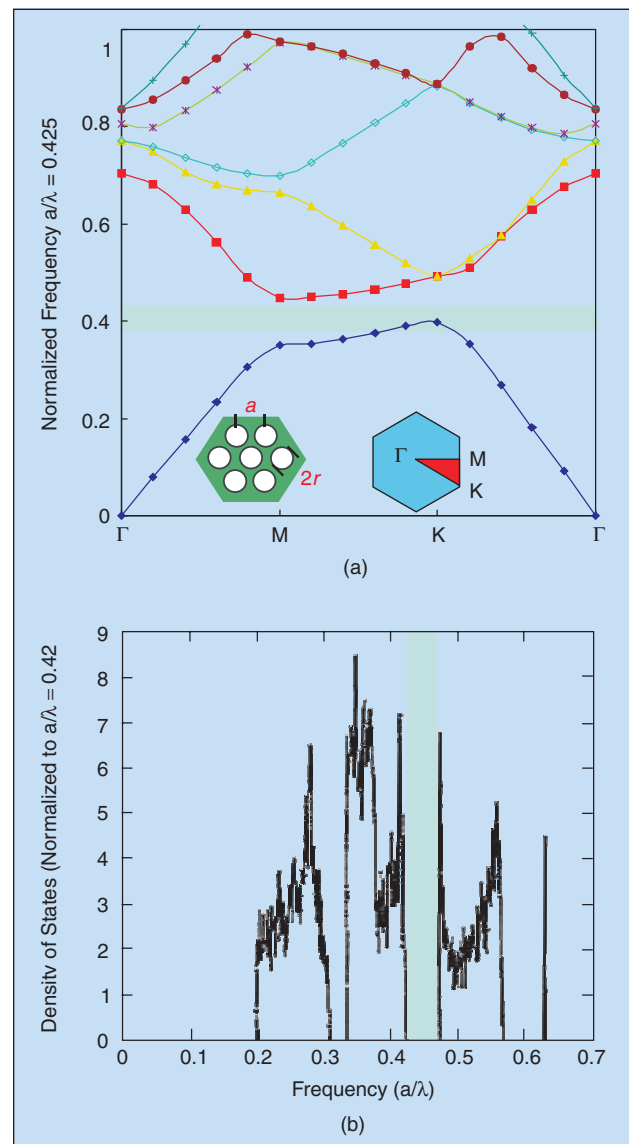
Microcavities realized by oxide confinement or by etching are usually accompanied by nonradiative defects resulting from such processing. An attractive technique to realize a true photonic microcavity is to use a dielectric photonic crystal, realized with a periodic modulation of the dielectric constant [5], [6]. As lightwaves scatter within a material with a periodic variation in the dielectric constant, destructive interference of certain frequencies, depending on geometry and index variation, produces a photonic bandgap (PBG) [7]. Photons whose energies lie within the gap cannot propagate through the structure. However, a point defect (a missing period or phase slip) in the structure will locally trap photons and create a microcavity [8]-[17]. All the photons corresponding to the wavelength of the defect, generated by recombination in the PBG crystal or otherwise, will be funneled into the single resonant mode of the defect and this mode can propagate in the crystal. Such a single-mode microcavity light-emitting diode, with a spontaneous emission factor  $\beta \sim 1$ , can also be viewed as a *thresholdless laser*. However, there are important differences. In a microcavity, or defect, there is feedback of the dominant mode in all directions. Also, unlike a laser, in which the output is a result of mode competition and gain saturation, in a true microcavity there is only one mode that is emitted. The resonant defect mode is highly localized around the defect and can either propagate in the plane of the PBG crystal by tunneling or leak out in the vertical direction. Lasing with optical pumping from a microcavity formed by a single defect in the center of a disc-shaped photonic crystal was first demonstrated by Scherer and coworkers [15], [16], and we have recently reported room-temperature operation of a GaAs-based PBG microcavity surface emitting electroluminescent device [18]. The light-current (L-I) characteristics of this device are

GaAs	0.0574 $\mu\text{m}$	p	$3 \times 10^{18}$
Al <sub>0.8</sub> Ga <sub>0.2</sub> As	0.0863 $\mu\text{m}$	p	$3 \times 10^{18}$
GaAs	0.0574 $\mu\text{m}$	p	$3 \times 10^{18}$
Al <sub>0.96</sub> Ga <sub>0.04</sub> As	0.08815 $\mu\text{m}$	p	$3 \times 10^{18}$
Al <sub>0.3</sub> Ga <sub>0.7</sub> As	0.1234 $\mu\text{m}$	p	$3 \times 10^{17}$
In <sub>0.15</sub> Ga <sub>0.85</sub> As	7 nm	i	----
Al <sub>0.3</sub> Ga <sub>0.7</sub> As	8 nm	i	----
In <sub>0.15</sub> Ga <sub>0.85</sub> As	7 nm	i	----
Al <sub>0.3</sub> Ga <sub>0.7</sub> As	0.1234 $\mu\text{m}$	i	----
Al <sub>0.96</sub> Ga <sub>0.04</sub> As	0.08815 $\mu\text{m}$	n	$2 \times 10^{18}$
GaAs	0.0574 $\mu\text{m}$	n	$2 \times 10^{18}$
Al <sub>0.8</sub> Ga <sub>0.2</sub> As	0.0863 $\mu\text{m}$	n	$2 \times 10^{18}$
n+ GaAs (100) Substrate and Buffer			

1. Photonic crystal microcavity device heterostructure grown by metal-organic vapor phase epitaxy (MOVPE) on  $n^+$  GaAs substrate with two 70 Å In<sub>0.15</sub>Ga<sub>0.85</sub>As quantum wells in a  $\lambda$  cavity.

very different from conventional lasers, or even microcavity VCSELs. We believe that the devices can be best described as "few mode" LEDs. The concept of a threshold current, therefore, cannot be strictly applied, and instead, we see a gradual turn-on, as predicted [1].

In what follows, we will first describe the design and fabrication of a 2-D PBG crystal and microcavity, with a GaAs-based heterostructure as an example. The properties of these devices will be described and discussed. This is followed by a brief description of the characteristics of 1.55  $\mu\text{m}$  quantum-well devices and 1  $\mu\text{m}$  quantum-dot devices.



2. (a) Calculated TE bandstructure using plane-wave expansion techniques and effective index method for 2-D finite height triangular photonic crystal geometry with air holes surrounded by a region with effective index of 1.8 and  $(r/a)=0.32$  and  $d=0.35 \mu\text{m}$ . A second-order mode centered at a normalized frequency of  $(a/\lambda)=0.425$  corresponding to  $a=0.4 \mu\text{m}$  and  $\lambda=0.94 \mu\text{m}$  is shown; (b) calculated photonic density of states using full 3-D simulation of the finite height 2-D photonic crystal verifying the existence of the second-order gap centered at normalized frequency  $a/\lambda=0.42$ .

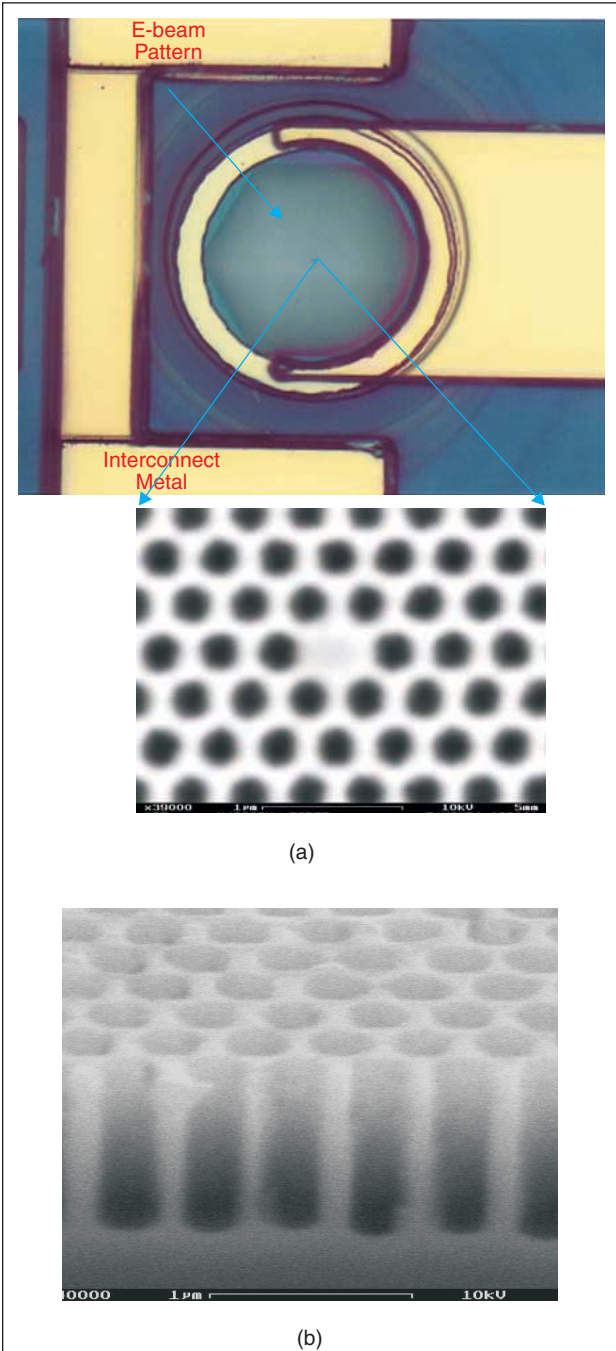
## Design and Fabrication of Photonic Bandgap Crystal Microcavity Light Emitters

In the electrically injected 2-D photonic crystal devices described in this article, we have 3-D confinement of light. In the horizontal direction the 2-D photonic crystal surrounding the defect microcavity provides the confinement. In the vertical direction, we have the air-semiconductor interface at the top and the semiconductor-DBR interface at the bottom of a  $\lambda$ -cavity slab to provide confinement. The vertical device heterostructure is shown in Figure 1. It consists of an undoped cavity region of thickness with two 70 Å pseudomorphic  $\text{In}_{0.15}\text{Ga}_{0.85}\text{As}$  quantum wells in the middle and p-type  $\text{Al}_{0.3}\text{Ga}_{0.7}\text{As}$  and contact layers on the top. N- and p-type  $\text{Al}_{0.96}\text{Ga}_{0.04}\text{As}$  layers are inserted for lateral wet-oxidation during the processing of the device. The reflectivity of the top surface is that provided by the semiconductor-air interface. The bottom DBR is not strictly required but is incorporated to achieve a high index step (reflectivity) in the bottom side and to ensure leakage of light from the top surface. Room-temperature photoluminescence (PL) measurements were done on the as-grown heterostructures. The peak in the luminescence occurs at 940 nm. The output is predominantly transverse-electric (TE) polarized due to the compressive strain in the InGaAs quantum wells. This is an advantage, since the PBG defect mode is predominantly TE polarized.

The photonic crystal configuration used in most defect microcavities is a triangular lattice of air holes etched into high refractive index material, in this case the GaAs-based heterostructure. It is found that this configuration has a relatively large gap for the TE modes [7]. The design of the photonic crystal defect microcavity is initiated with a suitable choice of the fill factor of the photonic crystal lattice determined by the ratio  $r/a$  where  $r$  is the radius of the air-holes and  $a$  is the lattice constant of the triangular lattice structure. A larger fill factor yields larger bandgaps [7] but fabrication considerations limit this value. Typically  $r/a$  values between 0.3-0.4 are optimum. In our design  $r/a=0.33$  was chosen. The operating wavelength  $\lambda$  is fixed by the vertical cavity design and the quantum-well active region emission, which was at 0.94  $\mu\text{m}$  in the heterostructure device. With  $\lambda$  and  $r/a$  fixed, the next step is to determine the bandstructure of the photonic crystal for TE modes and the normalized frequency  $a/\lambda$  of the defect mode within the bandgap. The finite thickness of the 2-D photonic crystal in the vertical direction, which for our  $\lambda$ -cavity structure is  $d=0.35 \mu\text{m}$ , has to be considered to accurately calculate the photonic crystal bandstructure. The simulations were done using the effective index method along with plane wave expansion techniques [19], [20]. The effective index calculations for the  $\lambda$ -cavity slab yield two modes (corresponding to two effective indices) with the second-order mode of the structure giving an effective index  $n_{\text{eff}}=1.8$ . This value was subsequently used to calculate the bandstructure of the photonic crystal using a 2-D plane wave expansion technique. As shown in Figure 2(a), we have a bandgap for the second-order mode for normalized frequency range  $a/\lambda$  between 0.39-0.43. The normalized frequency  $a/\lambda=0.425$  within this bandgap is chosen for our design encompassing the peak

emission of the quantum dots at  $\lambda=0.94 \mu\text{m}$  and fill factor  $r/a=0.33$ . The final design values for the photonic crystal are  $a=0.40 \mu\text{m}$  and  $r=0.13 \mu\text{m}$ .

The next stage in the design involved a full 3-D computation of the 2-D photonic crystal slab with a finite thickness (height). The design parameters of the structure as determined by the effective index method and plane-wave expansion techniques



3. (a) Photomicrograph and SEM images of top view of a fabricated device with top electrical ohmic contact surrounding the PBG with the single defect magnified in the inset; (b) cross-sectional SEM image of the 2-D PBG slab, with deep etching through the cavity down to the bottom DBR region.

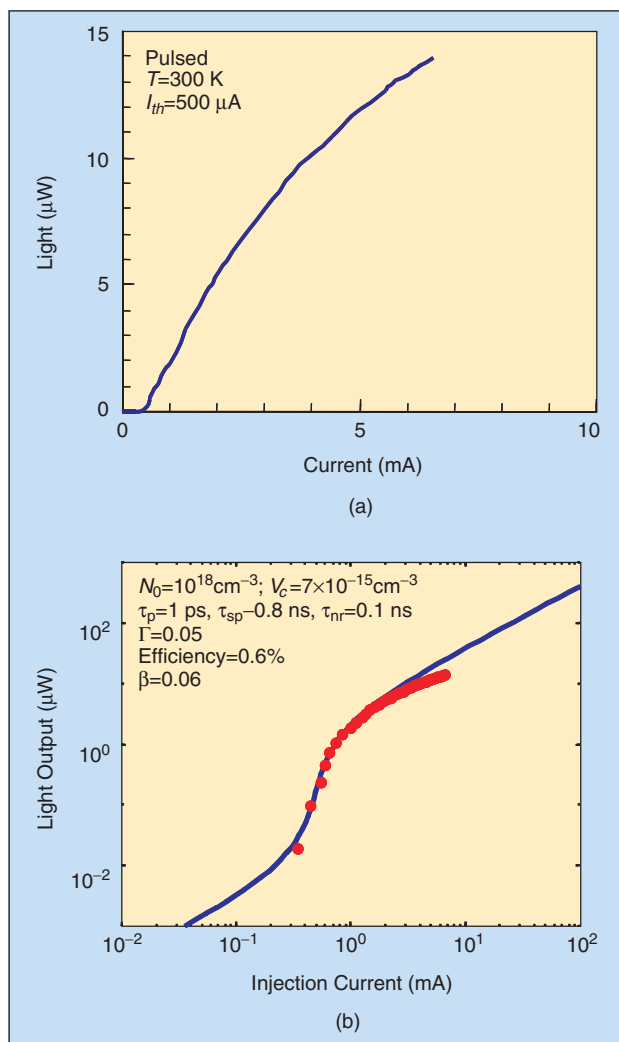


(namely,  $a$ ,  $r$ , and  $d$ ) are inserted in the 3-D calculations to verify the bandstructure. A purely analytical technique based on the separation of variables method was used to calculate the photon density of states of the structure. The electric field expressions in Maxwell's equation now contain a *nonzero*  $z$ -component ( $z$  direction being perpendicular to the photonic crystal slab surface), given by

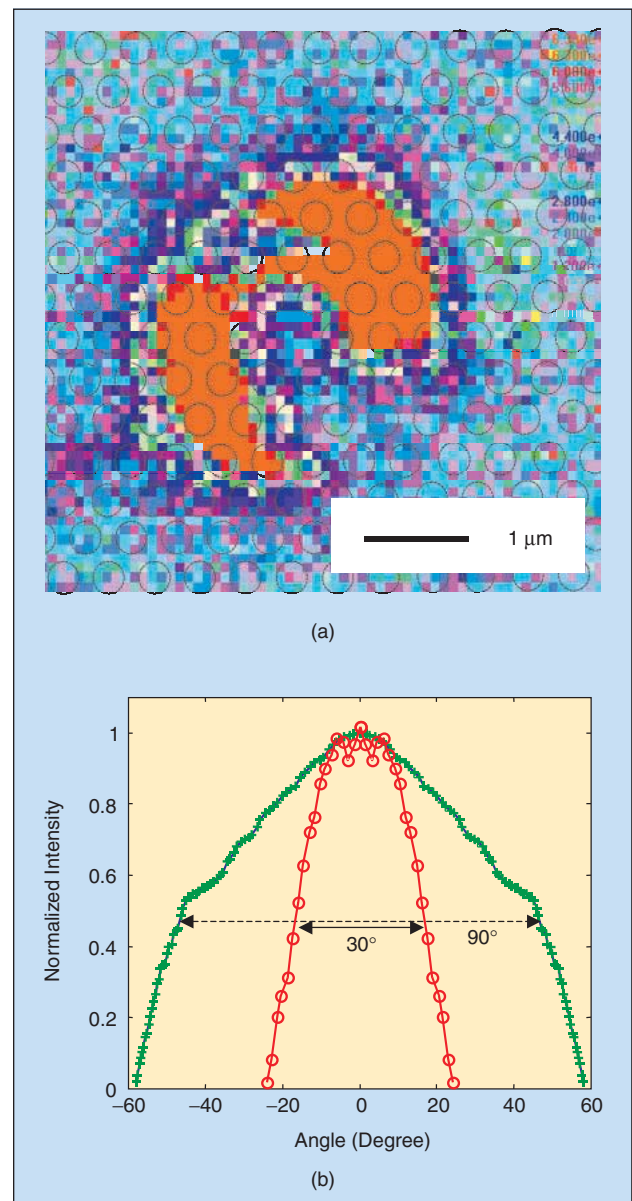
$$E_i(x, y, z) = \sum_G a_i(k + G) \exp[i(k + G) \cdot (x, y)] f_i(G, z) \quad (1)$$

where  $G$  is the reciprocal lattice vector and  $a_i$  and  $f_i$  are functions to be determined. The eigenvalue matrix contains  $z$ -derivatives of  $f_i$ . Next the boundary conditions for the air/dielectric surface of the slab are expressed in terms of  $f_i$  and its  $z$ -derivatives. The

resulting eigenvalue matrix along with the boundary conditions is treated as both an eigenvalue problem and a system of linear equations and solved self-consistently in an iterative process. Figure 2(b) shows the photon density of states for a finite 2-D photonic crystal slab obtained with first-, second- and third-order bandgaps occurring for normalized frequency ( $a/\lambda$ ) in the ranges 0.3-0.34, 0.41-0.46, and 0.56-0.62, respectively. Our final design, as indicated above, corresponds to an  $a/\lambda=0.425$  in the second-order gap of the photonic crystal and gives us the fabrication parameters  $a=0.4 \mu\text{m}$  and  $r=0.13 \mu\text{m}$ .



4. (a) Light-current characteristics of the GaAs-based single-defect PBG device at 300 K in pulsed mode showing a "soft" threshold current of 500  $\mu\text{A}$  and maximum power output of 14.4  $\mu\text{W}$ ; (b) rate equation analysis of the measured L-I characteristics for a GaAs-based single-defect photonic crystal microcavity light emitter, showing good agreement between the measured data (solid dots) and calculated values (solid lines). A good fit is obtained for a spontaneous emission factor  $\beta=0.06$ , which indicates strong spontaneous emission control and coherence in the output.



5. (a) Measured near-field image of the device output on the 2-D air-hole photonic crystal pattern at a distance of 4 mm from the surface of the device. The aperture defined by the wet-oxidized  $\text{Al}_{0.98}\text{Ga}_{0.02}\text{As}$  layer has a diameter of 40  $\mu\text{m}$ , which is much larger than the observed image; (b) measured far-field images before and after fabrication of photonic crystal. Linewidth of the pattern decreases from 90° to 30° with incorporation of a photonic crystal microcavity.

The fabrication of the electrically injected photonic crystal defect microcavity involves using standard photolithographic techniques and VCSEL processing to define the electrical contacts and oxide-confined apertures, followed by

e-beam lithography and deep dry etching techniques to subsequently define the photonic crystal with single or multiple defect regions in the center. The device heterostructure is first fabricated by optical lithography, dry and wet etching, metallization, and polyimide planarization to define the p and n contacts. Lateral wet-oxidation [21] of the  $\text{Al}_{0.96}\text{Ga}_{0.04}\text{As}$  layers was used here to funnel the charge carriers more efficiently into the center of the PBG region. Following this, the photonic crystal pattern is formed at the center of the mesa-etched apertures by e-beam lithography, pattern transfer, and deep dry etching techniques [22]. The window inside the oxide ring is measured to be  $\sim 40\text{ }\mu\text{m}$  in diameter. A single or multiple defect in the center defines the microcavity. A  $0.8\text{ }\mu\text{m}$  deep etch of the air-holes penetrates through the entire cavity region and well into the bottom DBR to ensure a good overlap with the optical field.

A photomicrograph of the complete device with p- and n-type contact metallizations is shown in Figure 3, together with scanning electron microscope (SEM) images of the PBG and the defect. The active area aperture, created by the single defect, is surrounded by over 40 periods of PBG, having an extent (radius) of  $20\text{ }\mu\text{m}$ , which also coincides with the current funneling aperture formed by wet oxidation of the  $\text{Al}_{0.96}\text{Ga}_{0.04}\text{As}$  layers.

### Device Characteristics

As mentioned earlier, the light-current (L-I) characteristics of these microcavity devices display unique properties. We have measured these characteristics in the pulsed mode. The output was measured in a direction normal to the surface. As seen in Figure 4(a) a turn-on, or “soft”-threshold-like behavior in the injection current, is consistently observed. The maximum output power that we have measured in these devices is  $14.4\text{ }\mu\text{W}$ . Care was taken to ensure that the measured power lies within the operating spectral and sensitivity ranges of the Ge detector, especially at low output powers. In order to understand the observed nature of the L-I characteristics near the region of the turn-on, or threshold, we have analyzed the data with the relevant carrier and photon rate equations [23]. As can be seen in Figure 4(b), good agreement between measured and calculated data is obtained for  $\beta \sim 0.06$  by taking into account a relatively large nonradiative surface recombination induced carrier loss ( $\tau_{sp} < \tau_{nr}$ ) and photon scattering loss in the device. A photon lifetime of  $1\text{ ps}$  and an optical confinement factor of  $0.05$  are used in the analysis. It may be noted that the value of  $\beta$ , although less

The fabrication of the electrically injected photonic crystal defect microcavity involves using standard photolithographic techniques and VCSEL processing to define the electrical contacts and oxide-confined apertures.

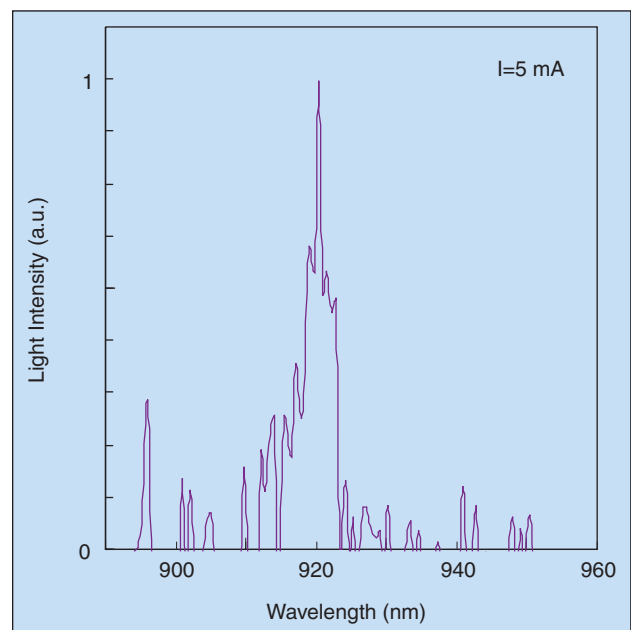
than unity, is significantly larger than that in conventional semiconductor lasers ( $\beta \sim 10^{-4}$ - $10^{-5}$ ).

It is evident that there is a certain amount of nonradiative surface recombination of the injected carriers that reach the defect

(microcavity) by traveling around the air-hole columns in the photonic crystal. Some carriers may also travel via the top surface. This region, defined by wet-oxidized AlGaAs layers, is  $40\text{ }\mu\text{m}$  in diameter. We estimate the total surface recombination current in these devices to be  $\sim 110\text{ }\mu\text{A}$ . For larger values of injection current, radiative processes dominate and the observed turn-on behavior represents true device characteristics.

### Near-Field, Far-Field, and Spectral Output Characteristics

“Near-field” imaging was accomplished at a distance of  $4\text{ mm}$  from the device surface and typical data are shown in Figure 5(a). It is evident that the modes spread out from the defect (microcavity) region during its propagation along the vertical direction. The nonuniformity in the mode profile is possibly due to light scattering in the air holes and diffraction at the surface [24]. Nonetheless, it is important to note that the  $4\text{ }\mu\text{m}$  lateral extent of the near-field image is much smaller than the oxide window diameter of  $40\text{ }\mu\text{m}$  and further helps to exclude the possibility that the entire 2-D PBG crystal beyond the defect microcavity contributes to the observed output. The field distribution and the localized defect mode in and around the defect in



6. Measured spectral output for the device at biasing currents of  $5\text{ mA}$ . The peak emission is at  $931\text{ nm}$  with a linewidth of  $\sim 8\text{ }\text{\AA}$ .

the photonic crystal were also calculated by the plane wave expansion and effective medium theory. The computations reveal that most of the energy of the defect mode leaks in the vertical ( $z$ ) direction, rather than being guided in the plane ( $x$ - $y$ ) of the photonic crystal. The modes are predominantly TE, with a small contribution from unguided transverse magnetic (TM) modes. The measured near-field output is in fair agreement with the calculated modal characteristics.

It may also be noted that the quantum-well emission overlaps with the bottom of the air band at the M point, and this emission

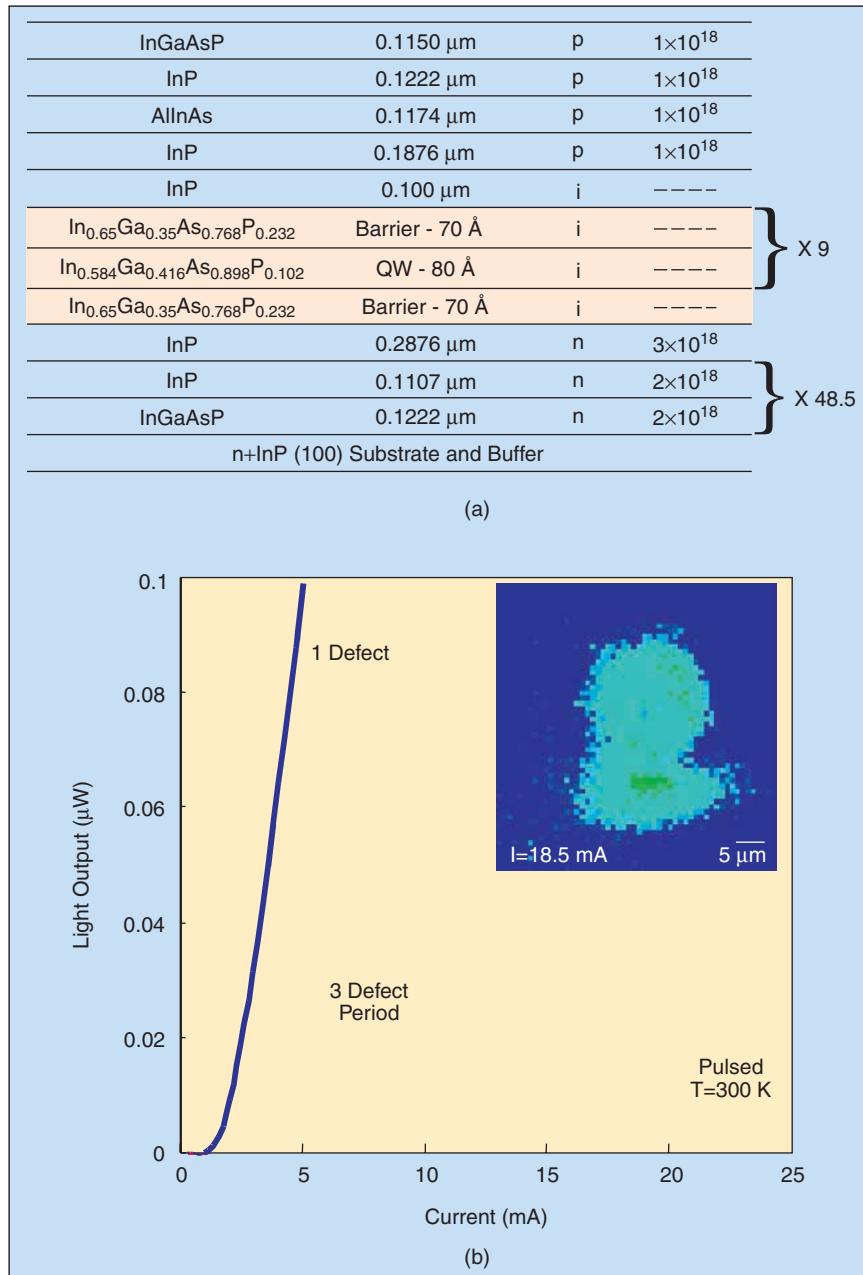
can, therefore, couple with the air-band-guided modes propagating in the  $\Gamma$ M direction. The near-field image indicates increased leakage in the  $\Gamma$ M direction. However, it cannot be confirmed whether only the dipole defect mode or a combination of defect and air-band modes are observed.

The output spectral characteristics, also measured in the pulsed mode with probe contacts above the turn-on point in the L-I curve, are shown in Figure 6. The main peak at 931 nm has a linewidth of 8 Å. This output wavelength corresponds to a normalized frequency  $a/\lambda=0.43$ , which is within the second-order gap of the photonic crystal.

We estimate the  $Q$ -value to be  $\sim 200$ . With this value of  $Q$  and a calculated effective modal volume  $V_{\text{eff}} \sim 3(\lambda/2n)^3$ , a spontaneous emission enhancement factor (Purcell factor) of 15 is derived [25], [26]. This value is reasonable for these devices. The far-field characteristics were also measured, to examine the expected directionality in the output. As shown in Figure 5(b), the linewidth (full width at half-maximum) of the pattern is  $\sim 30^\circ$ , in contrast to  $90^\circ$  for larger oxide-confined light emitting diodes, confirming that the observed light output originates from the single-defect microcavity. The output of these devices is also weakly polarized, exhibiting a preferential polarization direction. Ideally, a linearly polarized output is expected.

### Long Wavelength (1.55 $\mu\text{m}$ ) Devices

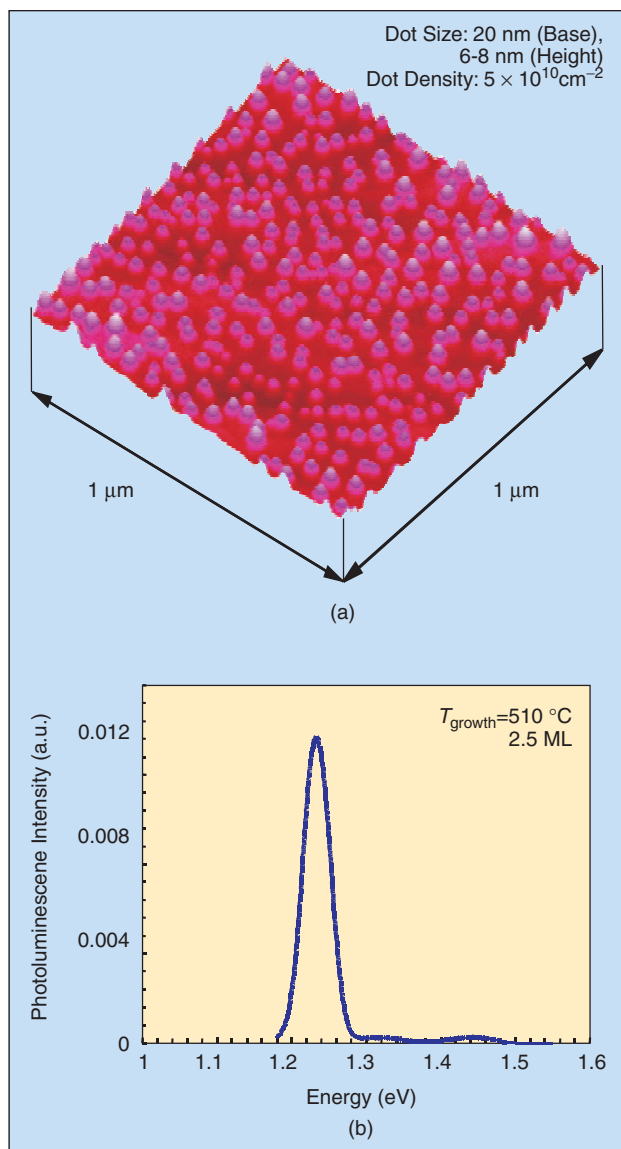
High-efficiency, reliable, and low-cost InP-based 1.55  $\mu\text{m}$  light emitters will continue to play an important role in the development of long-wavelength optical fiber communication systems. Vertical-cavity surface-emitting lasers (VCSELs) are promising devices because they potentially offer efficient fiber coupling, the capability of wafer-scale fabrication and testing, 2-D arrays, large packing densities, and low-voltage operation [27]. However, the development of long-wavelength VCSELs has lagged behind the shorter wavelength (0.8-1.0  $\mu\text{m}$ ) GaAs-based devices, mainly due to the difficulty involved in realizing suitable epitaxial mirrors. The low index contrast existing in lattice-matched InP-based heterostructures necessitates the growth of 40-50 pairs of hi-lo index materials to form the distributed Bragg reflector (DBR) at each end of the cavity. This invariably leads to a nonplanar device structure and difficulties



7. (a) Photonic crystal microcavity device heterostructure grown by MOVPE on  $n^+$  InP substrate with nine InGaAP quantum wells in a  $\lambda$ -cavity for 1.55  $\mu\text{m}$  emission; (b) L-I (pulsed mode) characteristics of a single-defect microcavity, with a "soft" threshold at  $I=1$  mA, and a three-defect period device. An increase in the slope efficiency by a factor of 22 is observed. Inset shows the measured near-field image obtained from a single-defect microcavity.

in processing. While other technologies are being explored [28]-[30] for long wavelength VCSELs, an alternative approach would be to use the confinement effects of photons in a microcavity light-emitting diode (MCLED) [1]-[3], [31], [32].

The design procedure of the photonic crystal microcavity is identical to that for the 0.9  $\mu\text{m}$  device described earlier. We have a bandgap for the second-order mode for normalized frequency range  $a/\lambda$  between 0.34-0.40. The normalized frequency  $a/\lambda=0.39$  within this bandgap is chosen for our design encompassing the peak emission of the quantum wells at  $\lambda=1.55 \mu\text{m}$  and fill factor  $r/a=0.33$ . The final design values for the photonic crystal are  $a=0.60 \mu\text{m}$  and  $r=0.2 \mu\text{m}$ . The InP-based heterostructure used to fabricate the device is shown in Figure 7(a). The active area aperture, created by the single defect, is  $0.8 \mu\text{m}$ . This aperture is surrounded by 65 periods of photonic crystal, having an extent (radius) of  $30 \mu\text{m}$ .



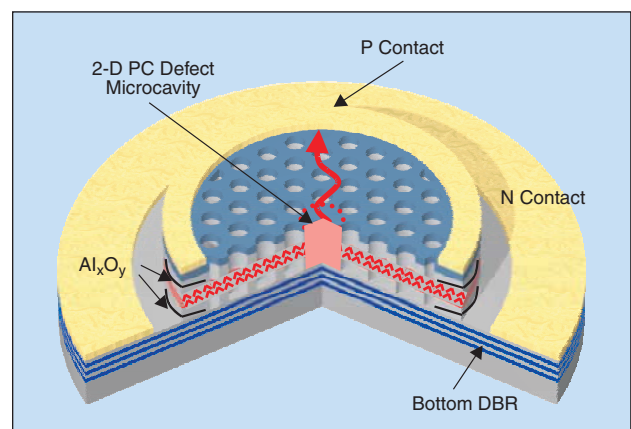
8. (a) Atomic force microscopy (AFM) image and (b) typical photoluminescence spectra of self-assembled InAs/GaAs quantum dots grown by molecular beam epitaxy.

The light-current characteristics of single-defect and three-defect devices have been measured in the pulsed mode and the results are shown in Figure 7(b). The single-defect device exhibits a maximum output power of  $\sim 1 \mu\text{W}$  and the characteristic soft threshold behavior is observed. From a rate equation analysis, a value of  $\beta=0.01$  is derived. It is important to note that the slope efficiency of the single-defect device is 22 times that of the three-defect one, signifying the dominance of microcavity effects. The output spectral characteristics of these devices could not be measured due to the low output power, but the measured near-field characteristics in the inset of Figure 7(b) distinctly show the light emission to originate from the microcavity region. The lateral extent of the output image, even at a distance of 4 mm, is much smaller than the oxide aperture of  $\sim 45 \mu\text{m}$  diameter.

### Future Prospects: Quantum Dot Devices and Arrays

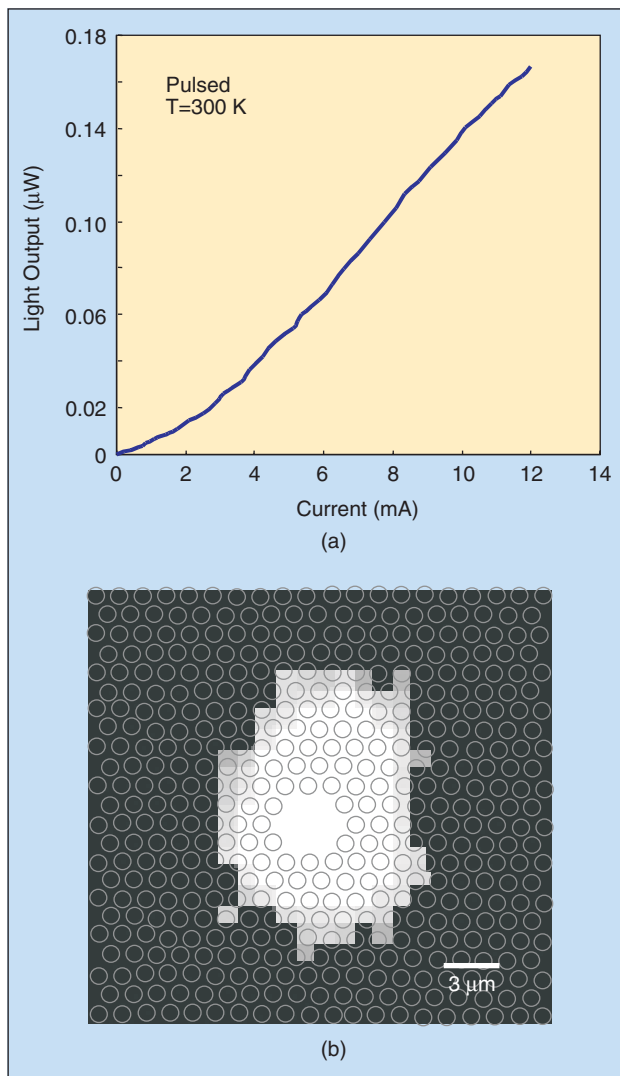
In the devices described above, the radiating element is a quantum well. It is conceivable that the active photon-emitting medium could be quantum dots and a cavity formed by a single defect would have, at best, a few dots. Such quantum-dot microcavity light-emitting diodes offer some unique advantages, including carrier and photon confinement in the same region, small optical loss, and a closer match of the narrow quantum dot emission linewidth with near-singular photon density of states. Such a device would also be a good vehicle to study effects related to quantum entanglement and single-photon emitters. Optically pumped photonic crystal microcavities with quantum dot active regions have been demonstrated recently [33], [34]. The properties of an electrically injected device are described in the following.

Highly lattice-matched (mismatch  $\geq 1.8\%$ ) Ga(In)As epitaxially grows on GaAs in the Stranski-Krastanow[35] growth mode, where self-organized islands are formed after a few monolayers of layer-by-layer growth [36]-[39]. For typical growth parameters used in MBE or MOVPE, an array of islands of lateral size 15-25 nm and heights 5-8 nm are formed. The coherently strained islands are, in essence, quantum dots. Elastic relaxation in the facet edges, renormalization of the surface energy



9. Schematic of single-defect electrically injected quantum dot photonic crystal microcavity light-emitting diode.





10. (a) L-I characteristics and (b) near-field images measured from a two-defect period quantum dot photonic crystal microcavity light-emitting diode. The near-field image shows that the emission is confined to the microcavity and few periods surrounding the cavity.

of the facets, and interaction between neighboring islands via the substrate are the driving forces for self-organized growth. The optical properties and luminescence efficiencies of these dots far surpass those of quantum dots realized by selective etching of epitaxially grown quantum wells [40]. An atomic force microscopy (AFM) image of InAs/GaAs quantum dots grown at the University of Michigan is shown in Figure 8(a). Typical dot densities lie in the range  $(1\text{--}10) \times 10^{10} \text{ cm}^{-2}$ . Theoretical band-structure calculations [41] and a variety of experimental techniques, including photoluminescence [42] and electroluminescence [43], reveal that there are a number of near-degenerate hole states and a few discrete electron states in the dots. Of these, the dominant ground and the first excited electron states are separated by 50–100 meV, depending on dot material, composition, heterostructure, and growth parameters used. The ground state is two-fold degenerate, whereas the first excited states are almost four-fold degenerate [41]. Typical luminescence spectra

of InAs/GaAs dots, with a ground state transition energy of  $\sim 1\mu\text{m}$ , are displayed in Figure 8(b).

A schematic of the single-defect photonic crystal quantum dot microcavity light-emitting diode, fabricated by the techniques described above, is shown in Figure 9. It is estimated that there are 500 dots in the microcavity volume. The photonic bandgap normalized frequency range  $a/\lambda$  is between 0.39–0.43. The normalized frequency  $a/\lambda=0.41$  within this bandgap is chosen for our design encompassing the peak emission of the quantum dots at  $\lambda = 1.04 \mu\text{m}$  and fill factor  $r/a=0.35$ . The final design values for the photonic crystal are  $a=0.42 \mu\text{m}$  and  $r=0.15 \mu\text{m}$ . The light-current characteristics of a two-defect microcavity device are shown in Figure 10(a). The light output is very small due to the small number of dots within the microcavity contributing to the photon emission and the surface recombination of injected carriers in these devices. The near-field image of the output, shown in Figure 10(b), unmistakably indicates photon emission from the quantum-dot microcavity.

Since the light output is small from a single microcavity device, it is conceivable that a closely spaced array, where each device is separated by  $\sim 20$  periods ( $8 \mu\text{m}$ ) of the photonic crystal, will give larger light output. The crystal periodicity could also be varied between successive elements, to provide a tunable array.

The devices described here have, by no means, been perfected. However, it is evident that by improving the technology somewhat, high-efficiency coherent single- or few-mode LEDs can be realized.

## Acknowledgment

The work is being supported by the Army Research Office under Grant DAAD 19-01-1-0527.

P. Bhattacharya (e-mail: pkb@eecs.umich.edu) is the James R. Mellor Professor of Engineering and J. Sabarinathan and P-C. Yu are research assistants at the University of Michigan's Department of Electrical Engineering and Computer Science in Ann Arbor, Michigan. W-D. Zhou, a recent graduate from the University of Michigan, is a member of the technical staff at Ciena Corporation, Linthicum, Maryland. A. McGurn is a professor in the Department of Physics, Western Michigan University, Kalamazoo, Michigan.

## References

- [1] H. Yokoyama, "Physics and device applications of optical microcavities," *Science*, vol. 256, pp. 66–70, Apr. 1992.
- [2] H. Benisty, J. Gerard, R. Houdré, J. Rarity, and C. Weisbuch, Eds., *Confined Photon Systems: Fundamentals and Applications*. New York: Springer, 1999.
- [3] T. Baba, "Photonic crystals and microdisk cavities based on GaInAsP-InP system," *IEEE J. Select. Topics Quantum Electron.*, vol. 3, pp. 808–830, June 1997.
- [4] I. Vurgaftman and J. Singh, "Spatial and spectral characteristics of spontaneous emission from semiconductor quantum wells in microscopic cylindrical cavities," *Appl. Phys. Lett.*, vol. 67, pp. 3865–3867, 1995.
- [5] E. Yablonovitch, "Inhibited spontaneous emission in solid-state physics and electronics," *Phys. Rev. Lett.*, vol. 58, pp. 2059–2062, 1987.



- [6] E. Yablonovitch, "Photonic band-gap structures," *J. Opt. Soc. Amer. B*, vol. 10, pp. 283-295, 1993.
- [7] J.D. Joannopoulos, R.D. Meade, and J.N. Winn, *Photonic Crystals*. Princeton, NJ: Princeton Univ. Press, 1995.
- [8] P. Villeneuve, S. Fan, and J.D. Joannopoulos, "Microcavities in photonic crystals: Mode symmetry, tunability, and coupling efficiency," *Phys. Rev. B*, vol. 54, pp. 7837-7842, 1996.
- [9] S. Lin, V. Hietala, S. Lyo, and A. Zaslavsky, "Photonic band gap quantum well and quantum box structures: A high-Q resonant cavity," *Appl. Phys. Lett.*, vol. 68, pp. 3233-3235, 1996.
- [10] D. Labilloy, H. Benisty, C. Weisbuch, T.F. Krauss, C.J.M. Smith, R. Houdré, and U. Oesterle, "High-finesse disk microcavity based on a circular Bragg reflector," *Appl. Phys. Lett.*, vol. 73, pp. 1314-1316, 1998.
- [11] A. Shaw et al., "Lasing properties of disk microcavity based on a circular Bragg reflector," *Appl. Phys. Lett.*, vol. 75, pp. 3051-3053, 1999.
- [12] A. Mekis, M. Meier, A. Dodabalapur, R.E. Slusher, and J.D. Joannopoulos, "Lasing mechanism in two-dimensional photonic crystal lasers," *Appl. Phys. A*, vol. 69, pp. 111-114, 1999.
- [13] M. Imada, S. Noda, A. Chutinan, T. Tokuda, M. Murata, and G. Sasaki, "Coherent two-dimensional lasing action in surface emitting laser with triangular-lattice photonic crystal structure," *Appl. Phys. Lett.*, vol. 75, pp. 316-318, 1999.
- [14] K. Inoue, M. Sasada, J. Kawamata, K. Sakoda, and J. Haus, "A two-dimensional photonic crystal laser," *Jpn. J. Appl. Phys.*, vol. 38, pp. L157-L159, 1999.
- [15] O. Painter, R.K. Lee, A. Yariv, A. Scherer, J.D. O'Brien, P.D. Dapkus, and I. Kim, "Two-dimensional photonic band-gap defect mode laser," *Science*, vol. 284, pp. 1819-1821, June 1999.
- [16] O. Painter, J. Vuckovic, and A. Scherer, "Defect modes of a two-dimensional photonic crystal in optically thin dielectric slab," *J. Opt. Soc. Amer. B*, vol. 16, pp. 275-285, 1999.
- [17] J. Hwang, H. Ryu, D. Song, I. Han, H. Song, H. Park, Y. Lee, and D. Jang, "Room-temperature triangular-lattice two-dimensional photonic bandgap lasers operating at 1.54  $\mu\text{m}$ ," *Appl. Phys. Lett.*, vol. 76, pp. 2982-2984, 2000.
- [18] W.D. Zhou, J. Sabarinathan, P. Bhattacharya, B. Kochman, E. W. Berg, P.C. Yu, and S.W. Pang, "Characteristics of a photonic bandgap single defect microcavity electroluminescent device," *IEEE J. Quantum Electron.*, vol. 37, pp. 1153-1160, Sept. 2001.
- [19] C. Pollock, *Fundamentals of Optoelectronics*. Chicago, IL: Irwin, 1995.
- [20] R.D. Meade, A.M. Rappe, K.D. Brommer, J.D. Joannopoulos, and O.L. Alerhand, "Accurate theoretical analysis of photonic band-gap materials," *Phys. Rev. B*, vol. 48, pp. 8434-8437, 1993.
- [21] J.M. Dallesasse, N. Holonyak Jr., S.R. Sugg, T.A. Richard, and N. El-Zein, "Hydrolyzation oxidation of Al Ga As-AlAs-GaAs quantum well heterostructures and superlattices," *Appl. Phys. Lett.*, vol. 57, pp. 2844-2846, 1990.
- [22] E. Berg and S.W. Pang, "Cl plasma passivation of etch induced damage in GaAs and InGaAs with an inductively coupled plasma source," *J. Vac. Sci. Tech. B*, vol. 17, pp. 2745-2749, 1999.
- [23] G. Bjork and Y. Yamamoto, "Analysis of semiconductor microcavity lasers using rate equations," *IEEE J. Quantum Electron.*, vol. 27, pp. 2386-2396, Nov. 1991.
- [24] D. Ochoa, R. Houdré, M. Ilegems, H. Benisty, T.F. Krauss, and C.J.M. Smith, "Diffraction of cylindrical Bragg reflectors surrounding an in-plane semiconductor microcavity," *Phys. Rev. B*, vol. 61, pp. 4806-4812, 2000.
- [25] R. Coccioli, M. Boroditsky, K.W. Kim, Y. Rahmat-Samii, and E. Yablonovitch, "Smallest possible electromagnetic mode volume in a dielectric cavity," *Proc. Inst. Electr. Eng. - Optoelectron.*, vol. 145, pp. 391-397, 1998.
- [26] M. Boroditsky, R. Vrijen, T.F. Krauss, R. Coccioli, R. Bhat, and E. Yablonovitch, "Spontaneous emission extraction and Purcell enhancement from thin-film 2-D photonic crystals," *J. Lightwave Technol.*, vol. 17, pp. 2096-2112, 1999.
- [27] C. Wilmsen, H. Temkin, and L.A. Coldren, eds., *Vertical-Cavity Surface-Emitting Lasers: Design, Fabrication, Characterization, and Applications*. Cambridge, UK: Cambridge Univ. Press, 1999.
- [28] T. Baba, Y. Yogo, K. Suzuki, F. Koyama, and K. Iga, "Near room temperature continuous wave lasing characteristics of GaInAsP/InP surface emitting laser," *Electron. Lett.*, vol. 29, pp. 913-915, 1993.
- [29] J. Dudley, D.I. Babic, R. Mirin, L. Yang, B.I. Miller, R.J. Ram, T. Reynolds, E.L. Lu, and J.E. Bowers, "Low threshold wafer-fused long wavelength vertical cavity lasers," *Appl. Phys. Lett.*, vol. 65, pp. 1463-1465, 1994.
- [30] N.M. Margalit, J. Piprek, S. Zhang, D.I. Babic, K. Streubel, R.P. Mirin, J.R. Wesslmann, J.E. Bowers, and E.L. Hu, "64° C continuous-wave operation of a 1.54  $\mu\text{m}$  vertical-cavity lasers," *IEEE J. Select. Topics Quantum Electron.*, vol. 3, pp. 359-365, 1997.
- [31] E.F. Schubert, N.E.J. Hunt, M. Micovic, R.J. Malik, D.L. Sivco, A.Y. Cho, and G.J. Zydzik, "Highly efficient light-emitting diodes with microcavities," *Science*, vol. 265, pp. 943-945, Aug. 1994.
- [32] H. De Neve, J. Blondelle, R. Baets, P. Demeester, P. Van Daele, and G. Borghs, "Resonant cavity LED's," in *Microcavities and Photonic Bandgaps*, J. Rarity and C. Weisbuch, Eds. Norwell, MA: Kluwer, 1996, pp. 333-342.
- [33] C. Reese, C. Becher, A. Imamoglu, E. Hu, B. Gerardot, and P. Petroff, "Photonic crystal microcavities with self-assembled InAs quantum dots as active emitters," *Appl. Phys. Lett.*, vol. 78, pp. 2279-2281, 2001.
- [34] T. Yoshie, A. Scherer, H. Chen, D. Huffaker, D. Deppe, "Optical characterization of two-dimensional photonic crystal cavities with indium arsenide quantum dot emitters," *Appl. Phys. Lett.*, vol. 79, pp. 114-116, 2001.
- [35] I.N. Stranski and L. Krastanow, in *Proc. Academy of Sciences Vienna*, Dept. IIb, vol. 146, pp. 797, 1937.
- [36] P.R. Berger, K. Chang, P. Bhattacharya, J. Singh, and K.K. Bajaj, "Role of strain and growth conditions on the growth front profile of  $\text{In}_{0.4}\text{Ga}_{0.6}\text{As}$  on GaAs during the pseudomorphic growth regime," *Appl. Phys. Lett.*, vol. 53, p. 684, 1988.
- [37] M. Tabuchi, S. Noda, and A. Sasaki, "Strain energy and critical thickness of heteroepitaxial InGaAs layers on GaAs substrate," *J. Cryst. Growth*, vol. 115, p. 169, 1991.
- [38] Q. Xie, P. Chen, A. Kalburge, T.R. Ramachandran, A. Nayfonov, A. Konkar, and A. Madhukar, "Realization of optically active strained InAs island quantum boxes on GaAs (100) via molecular beam epitaxy and the role of island induced strain fields," *J. Cryst. Growth*, vol. 150, p. 357, 1995.
- [39] D. Leonard, M. Krishnamurthy, C.M. Reeves, S.P. Denbaars, and P.M. Petroff, "Direct formation of quantum-sized dots from uniform coherent islands of InGaAs on GaAs surfaces," *Appl. Phys. Lett.*, vol. 63, pp. 3202, 1993.
- [40] F.E. Prins, G. Lehr, M. Burkard, S. Nikitin, H. Schweizer, and G. Smith, "Quantum dots and quantum wires with high optical quality by implantation-induced intermixing," *Jpn. J. Appl. Phys.*, vol. 32, pp. 6228, 1993.
- [41] H. Jiang, and J. Singh, "Strain distribution and electronic spectra of InAs/GaAs self-assembled dots: An eight-band study," *Phys. Rev. B*, vol. 56, p. 4696, 1996.
- [42] Y. Toda and Y. Arakawa, "Near-field spectroscopy of a single InGaAs self-assembled quantum dot," *IEEE J. Select. Topics Quantum Electron.*, vol. 6, p. 528, May-June 2000.
- [43] D.L. Huffaker, and D.G. Deppe, "Electroluminescence efficiency of 1.3  $\mu\text{m}$  wavelength InGaAs/GaAs quantum dots," *Appl. Phys. Lett.*, vol. 73, pp. 520, 1998.

CD ■